EDGE ARTICLE

Check for updates

Bisphosphonium cation based metal halide glass scintillators with tunable melting points†‡

Jian-Bin Luo,§ Jun-Hua Wei,§ Zi-Lin He, Jing-Hua Chen, Qing-Peng Peng, Zhi-Zhong Zhang and Dai-Bin Kuang ⓘD *

Organic–inorganic metal halide (OIMH) glass offers the advantages of large-scale production, high transparency, and minimal light scattering. However, undesired crystallization in OIMH glass can occur, leading to deteriorated transparency. Herein, a series of bisphosphonium organic cations were designed to construct Mn-based metal halide crystals with a photoluminescence quantum yield (PLQY) near unity, alongside the development of highly thermally stable OIMH glasses. Two strategies were employed to lower the melting point of OIMH: alkyl chain elongation and fluorine substitution. The (Hex-3,4-2F) $MnBr_4 \cdot MeOH$ (Hex-3,4-2F = hexane-1,6-diylbis((3,4-difluorobenzyl)diphenylphosphonium)) crystal delivers a glass transition temperature of 100 °C and the highest T_g/T_m ratio (0.82) among OIMHs. The resulting OIMH glass exhibits a PLQY of 47.6%, achieves an impressive resolution of 25 lp mm^{-1} in X-ray imaging, and remains transparent even after being heated at 90 °C for six weeks. These bisphosphonium-based OIMH glasses present a feasible design for the practical application of OIMH glasses in radiation detection.

Introduction

Scintillators are a category of material capable of converting high-energy radiation into low-energy ultraviolet/visible light, serving as a crucial component in indirect X-ray detectors,[1,2] which play a vital role in high-energy physics research, medical radiography, and security inspections.[3,4] Currently, commercial scintillators such as thallium-doped cesium iodide (CsI: Tl), cerium-doped lutetium aluminum garnet (LuAG: Ce), and bismuth germanate (BGO) often require extremely high temperatures for preparation and, in some cases, exhibit strong hygroscopicity. Therefore, the development of novel, cost-effective, high-performance, and highly stable X-ray scintillators holds paramount significance.[5–11]

Organic–inorganic metal halide (OIMH) exhibits exceptional luminescent performance, holding promising prospects in solid-state lighting, backlight displays, optical anti-counterfeiting, radiation detection, and various other domains.[12–16] The commonly employed luminescent metal centers include Pb, Sn, Sb, Cu, Mn, and others. Mn-based metal halides, in particular, have attracted extensive attention due to

Key Laboratory of Bioinorganic and Synthetic Chemistry of Ministry of Education, LIFM, GBRCE for Functional Molecular Engineering, School of Chemistry, IGCME, Sun Yat-Sen University, Guangzhou 510275, China. E-mail: kuangdb@mail.sysu.edu.cn

† Dedicated to the 100th Anniversary of Sun Yat-sen University.

‡ Electronic supplementary information (ESI) available. CCDC 2349445–2349452. For ESI and crystallographic data in CIF or other electronic format see DOI: https://–doi.org/10.1039/d4sc04229h

§ Jian-Bin Luo and Jun-Hua Wei contributed equally to this work.

their high luminescent efficiency, cost-effectiveness, and low toxicity. Mn^{2+} ions can bond with halogen anions to form octahedral and tetrahedral units to present colorful emissions. The luminescent mechanism of Mn-based OIMH has been thoroughly investigated.[17] The highly localized excitons in low-dimensional Mn-based OIMH facilitate effective radiative recombination and yield remarkable PLQYs. Furthermore, the PLQY of Mn-based OIMH can easily approach nearly 100% by controlling the Mn–Mn distances and crystal field strength.

Despite the high PLQY and corresponding robust spacial resolution ($\geq$25 lp mm^{-1}) of Mn-based OIMH single crystals,[18,19] applying them in the field of radiation detection still faces a series of challenges: (1) the growth of single crystal is time-consuming and it is exceedingly difficult to control the morphology of OIMH *via* the solution method; (2) the ability to grow large-size single crystals is related to the inherent growth characteristics of the material, for which universal principles are lacking. Consequently, it is nearly impossible to obtain large-area OIMH single crystal scintillation screens of suitable dimensions. Increasing attention has been given to the glassy state of Mn-based OIMH,[20–22] since the first demonstration of large-area (10 cm × 10 cm) amorphous (HTPP)$_2$MnBr$_4$ (HTPP = hexyltriphenylphosphonium) glass prepared through a melt-quenching method by heating the crystal to form a melt and subsequently rapidly cooling it.[23] The OIMH glass is highly transparent with minimal light scattering, making it highly suitable to serve as a scintillator.[23–25]

Preparing OIMH glass *via* the melt-quenching method requires two essential prerequisites: (1) the melting temperature should be below the decomposition temperature to prevent

OIMH from decomposing before melting. (2) No crystallization should occur during the quenching process. Engineering of the bulky organic cations provides opportunities to lower the melting point of OIMH, thus minimizing the risk of decomposition. Most of the reported OIMH glasses are based on phenyl phosphonium cations, which are characterized by weak interactions between cationic and anionic groups, resulting in lower melting points.[26,27] These phenyl phosphonium cations also exhibit favorable crystallization properties owing to the π–π stacking effect.[28,29] However, the pronounced crystallization ability of OIMH can facilitate the transformation from amorphous glass to crystalline form within a limited timeframe, complicating the production of highly stable amorphous glass. This recrystallization ultimately leads to devitrification and significant light scattering, posing challenges for OIMH glass to work as a promising scintillator.

The crystallization of amorphous glasses typically occurs in the supercooled liquid region, namely the temperature range between the glass transition temperature (T_g) and melting temperature (T_m) according to the crystallization theory of amorphous glasses.[30] Turnbull proposed the well-known criterion to evaluate the glass-forming ability (GFA), measured by the reduced temperature (T_{rg}: $T_{rg} = T_g/T_m$).[31] Subsequently, the "two-thirds rule" was introduced.[32,33] When T_{rg} exceeds 2/3, the crystallization nucleation is essentially inhibited due to the sluggishness of the crystallization kinetics.[34] A smaller T_{rg} implies a higher tendency for crystallization and a correspondingly higher crystallization rate.[35] Therefore, higher T_g and lower T_m are advantageous for improving the stability of amorphous glasses. In the case of OIMH glass, a common approach involves elongating the alkyl chain of organic cations to increase the cation size, thereby reducing T_m,[27] or adjusting metal and halogen ions to control T_g.[29]

The bisphosphonium organic cation refers to a cation containing two P cores possessing a more bulky structure. This configuration effectively separates the Mn(II) center, leading to the formation of localized luminescent centers and enhancing the luminescent efficiency. Furthermore, the increased steric hindrance during motion and heightened molecular rigidity of bulky organic cations result in a higher T_g. However, the lack of flexibility in bisphosphonium cations also leads to a high T_m (e.g. $T_m = 295\ °C$ for $((C_{38}H_{34}P_2)MnBr_4)$[36]) potentially leading to the partial decomposition of OIMH before melting. Therefore, there is an urgent need to develop new strategies to modulate OIMH properties, aiming to strike a balance between processing temperature, luminescent performance, and stability.

Herein, we develop a halide-substituted bisphosphonium cation strategy to construct a series of bisphosphonium-based manganese halide (BisPP)MnBr$_4$ (BisPP = bis-phosphonium) single crystals with strong glass-forming ability. By connecting two phenylphosphine cores with alkyl chains, we achieve a T_g significantly higher than that of monophosphonium cations. The melting point (T_m from 281 °C to 180 °C) and photoluminescence quantum efficiency (PLQY from 66.7% to 99.9%) of these OIMHs single crystals can be fine-tuned by varying the length of the alkyl chains and the substituent groups on the benzene rings. Notably, the prepared (Hex-3,4-2F)MnBr$_4$·MeOH

(Hex-3,4-2F = hexane-1,6-diylbis((3,4-difluorobenzyl)diphenylphosphonium)) crystal exhibits a T_m of only 180 °C, and a T_g of up to 100 °C. Remarkably, its T_{rg} is as high as 0.82, marking the highest value among the reported metal halides. Additionally, the corresponding melt-quenched glass demonstrates a notable PLQY of 47.6% and exceptional stability after being heated at 90 °C for six weeks without any indication of devitrification. The unprecedented spatial resolution (25 lp mm^{-1}) demonstrates significant promise in radiation detection and offers a practical strategy for designing highly stable OIMH glasses.

Results and discussion

The organic components of the OIMH were obtained through the substitution reactions of a series of diphosphine compounds with halocarbons in toluene (Scheme S1‡). The bisphosphine compounds used in this study include 1,4-bis(diphenylphosphino)butane, 1,5-bis(diphenylphosphino)pentane, and 1,6-bis(diphenylphosphino)hexane. The resulting benzylation white powders were washed with ethyl acetate and dried to remove the residual solvent, yielding the bisphosphonium bromide salts. These bisphosphonium cations are shown in Fig. 1a–c. Subsequently, the manganese metal halides single crystals were prepared through a solvothermal method at 100 °C (Scheme S2‡), which involved the direct reaction between the organic bisphosphonium bromide salt and MnBr$_2$·4H$_2$O. The resulting compounds are denoted as (But-bz)MnBr$_4$ (But-bz = butane-1,4-diylbis(benzyldiphenylphosphonium)), (Pent-bz)MnBr$_4$ (Pent-bz = pentane-1,5-diylbis(benzyldiphenylphosphonium)) and (Hex-bz)MnBr$_4$ (Hex-bz = hexane-1,6-diylbis(benzyldiphenylphosphonium)), respectively. As shown in Fig. 1d–f, all three compounds exhibit a zero-dimensional structure, with each Mn atom coordinated with four Br atoms, forming a tetrahedral cluster. These $[MnBr_4]^{2-}$ clusters are spatially separated by the bulky bisphosphonium organic cations, with inter-cluster distances exceeding 8 Å. This spatial arrangement effectively inhibits concentration-induced PL quenching, resulting in a higher PLQY. Detailed crystallographic data are provided in Table S1.‡ The agreement of experimental and simulated powder X-ray diffraction (PXRD) patterns (Fig. 1g) supports the validity of the crystal structure refinement.

To investigate the thermal properties of these (BisPP)MnBr$_4$ crystals, thermogravimetric analysis (TGA) and differential scanning calorimetry (DSC) were conducted. As displayed in Fig. S1a–c,‡ the decomposition temperatures (T_d) of (But-bz)MnBr$_4$, (Pent-bz)MnBr$_4$ and (Hex-bz)MnBr$_4$ were found to be 343, 346, and 342 °C, respectively. The high T_d of (BisPP)MnBr$_4$ prevents the pre-melt decomposition, which is a prerequisite for the preparation of glass by the melt-quenched method. The DSC curves in Fig. 1h reveal that the T_m of (But-bz)MnBr$_4$, (Pent-bz)MnBr$_4$ and (Hex-bz)MnBr$_4$ are 281, 268, and 225 °C, respectively, while their glass transition temperatures are 109, 102, and 98 °C correspondingly. In comparison to metal halides based on monophosphonium cations, these bisphosphonium-based metal halides exhibit higher T_g, T_m, and T_d. The bulky
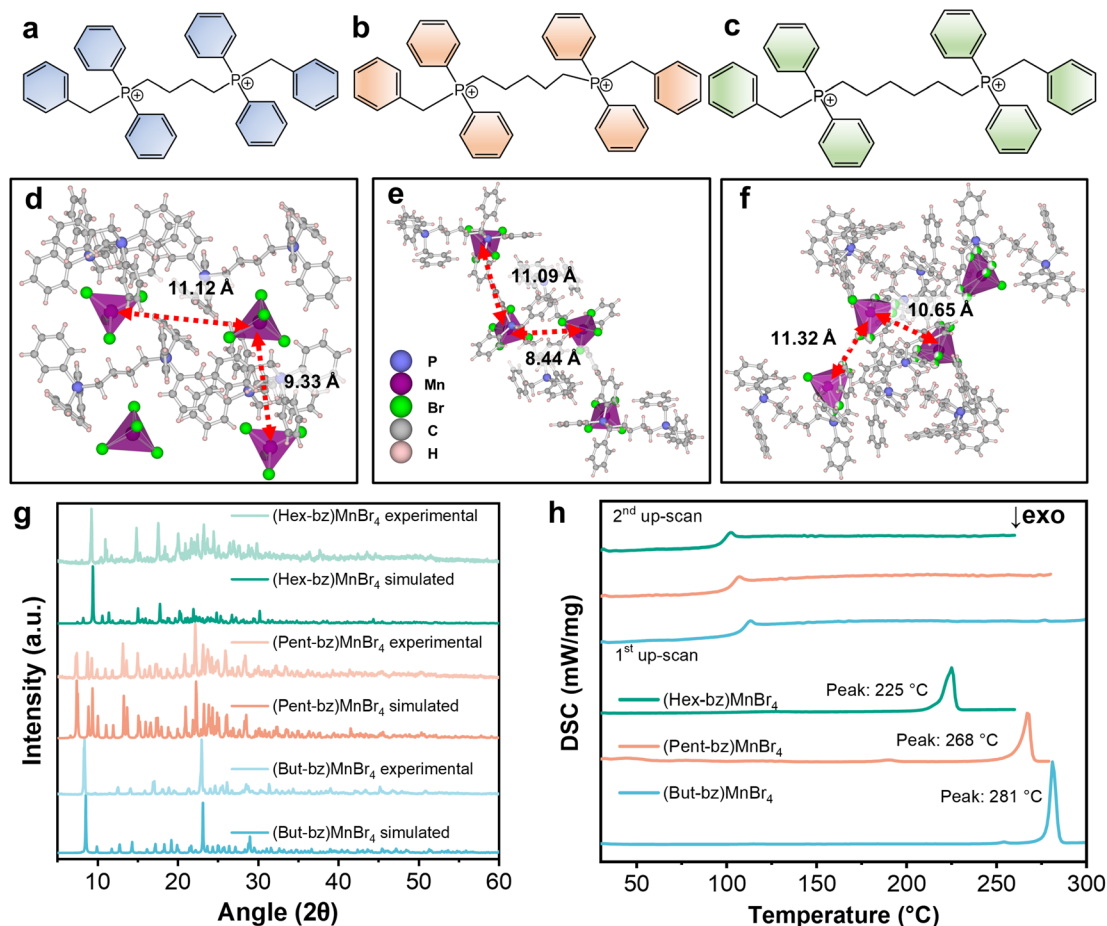
Fig. 1 (a–c) Structures of the bisphosphonium cations with different alkyl chain lengths. (a) But-bz; (b) Pent-bz; (c) Hex-bz. (d–f) Crystal structures of (d) (But-bz)MnBr$_4$; (e) (Pent-bz)MnBr$_4$; (f) (Hex-bz)MnBr$_4$ (grey: C, pink: H, blue: P, purple: Mn, green: Br). (g) Comparison of the simulated XRD and experimental XRD patterns. (h) Differential scanning calorimetry (DSC) of crystalline (But-bz)MnBr$_4$, (Pent-bz)MnBr$_4$, and (Hex-bz)MnBr$_4$, showing the first and second heating processes.

bisphosphonium cation substantially enhances the thermal stability of metal halides while simultaneously suppressing the crystallization behavior.[37] The elongation of the alkyl chains between the two phosphonium cores increases the flexibility of the bisphosphonium cations, which contributes to a decrease in both T_m and T_g. OIMH with quaternary phosphonium cations and metal-halide anions are considered ionic liquids in a broad sense, so the reduction of T_m is associated with the interactions between the anions and cations. As illustrated in Fig. S2,‡ the complexation strength between the bisphosphonium cation and the metal-halide anion weakens as the alkyl chain becomes longer, leading to a decrease in T_m.

The prepared (But-bz)MnBr$_4$, (Pent-bz)MnBr$_4$, and (Hex-bz) MnBr$_4$ crystals show bright greenish emission under 360 nm light. As shown in Fig. 2a, all three compounds exhibit single-peak emission. The luminescent lifetimes, presented in Fig. 2b, fall within the microsecond range. Furthermore, based on the photoluminescence excitation (PLE) spectrum in Fig. S3,‡ the green emission can be attributed to the characteristic emission of Mn^{2+} ions. Benefiting from large Mn–Mn distances, all three crystals deliver high PLQY values of 99.9%,

96.0%, and 66.7% respectively (Fig. 2c). The optical properties of the crystals are listed in Table S2.‡ Previous studies on bisphosphonium-based manganese halides have also demonstrated luminescent characteristics of isolated [MnBr$_4$]$^{2-}$ tetrahedra, confirming that bisphosphonium cations serve as effective spacers. Subsequently, we obtained the transparent OIMH glasses by melt-quenching these crystals (see the Materials and methods section for experimental details). The XRD patterns of the resulting OIMH glasses exhibit broad diffraction peaks, indicating a long-range disordered structure (Fig. S4‡). Fourier transform infrared spectroscopy (FTIR) confirms that the corresponding OIMH crystal and glass share the same organic matrix (Fig. 2d). Furthermore, the Raman spectra reveal that both the OIMH crystal and glass contain similar [MnBr$_4$]$^{2-}$ tetrahedra (Fig. 2e). The peaks observed in the 50–300 cm^{-1} range of the Raman spectra can be attributed to the vibrations of metal–halogen bonds, while those in the 500–4000 cm^{-1} range are associated with the vibrations of organic cations. The PL and PLE spectra of the OIMH glasses, shown in Fig. S5,‡ also exhibit characteristics of the emission of Mn^{2+}. The results indicate that the OIMH glasses prepared through the melt-
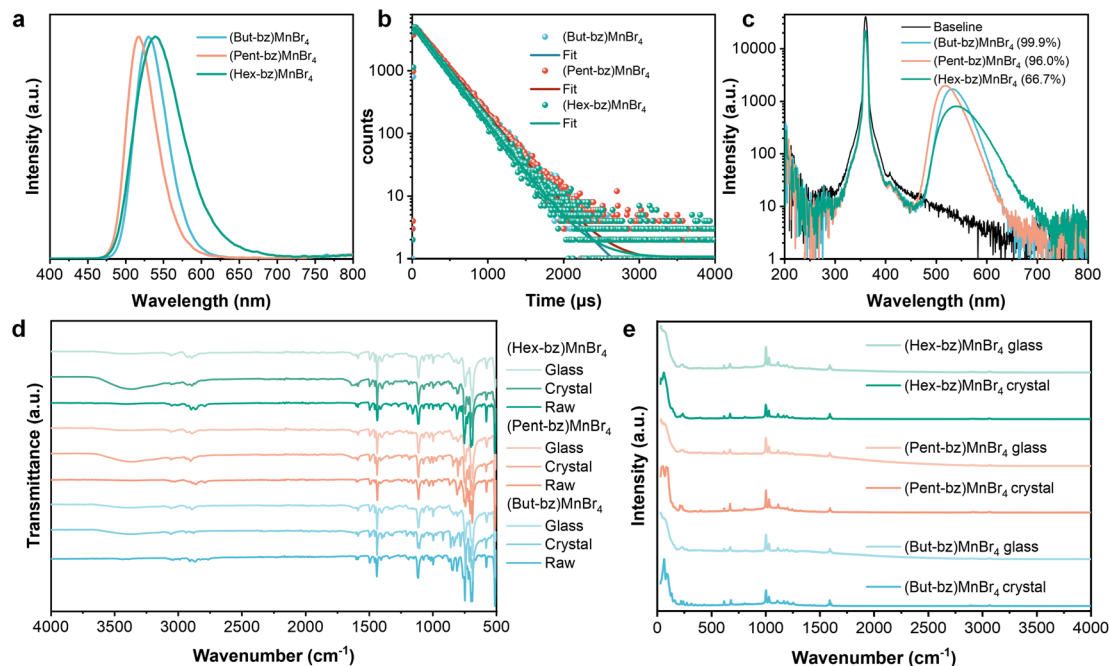
Fig. 2 (a) The emission spectra of (But-bz)MnBr$_4$, (Pent-bz)MnBr$_4$, (Hex-bz)MnBr$_4$ crystals under 360 nm excitation. (b) The time-resolved photoluminescence decay curves of (But-bz)MnBr$_4$, (Pent-bz)MnBr$_4$, and (Hex-bz)MnBr$_4$ crystals. (c) PLQY plots of (But-bz)MnBr$_4$, (Pent-bz) MnBr$_4$, and (Hex-bz)MnBr$_4$ crystals. (d) Attenuated total reflectance (ATR)-Fourier transform infrared spectra of (BisPP)MnBr$_4$ crystals and glasses. The plot labeled *Raw* means the corresponding bisphosphonium bromide salts (BisPP–Br). (e) Raman spectra of (BisPP)MnBr$_4$ crystals and glasses.

quenching method feature an amorphous nature when compared to their crystalline counterparts. As shown in Fig. S6a–c,‡ the DSC curves of (But-bz)MnBr$_4$ and (Pent-bz) MnBr$_4$ glasses show exothermic cold crystallization peaks during heating, followed by a remelting peak. In contrast, the (Hex-bz)MnBr$_4$ glass does not exhibit cold crystallization, suggesting its superior stability relative to (But-bz)MnBr$_4$ and (Pent-bz)MnBr$_4$ glasses. The glass transition temperature, surpassing room temperature, also indicates the ability of the melt-quenched glass to operate stably at ambient conditions.

Despite the similar compositions of these three compounds, the PLQY of (Hex-bz)MnBr$_4$ (66.7%) is lower than that of (But-bz)MnBr$_4$ (99.9%) and (Pent-bz)MnBr$_4$ (96.0%). Additionally, the full width at half maximum (FWHM) of (Hex-bz)MnBr$_4$ is broader, indicating the significant differences in the crystal field within this compound.[38] The ground state of Mn^{2+} is represented by $^6A_1$, and its excitation and de-excitation processes involve the spin flip of excited electrons. We employed DFT calculation to simulate the ground- and excited-state electronic configurations of these three crystals, as illustrated in Fig. S7.‡ For the ground states of all three compounds (Fig. S7a–c‡), the alpha HOMO orbitals are primarily contributed by Mn and Br, while the beta LUMO orbitals are mainly constituted by C and P. To investigate the origin of the PLQY difference, we simulated the excited dynamic of electrons on Mn^{2+}. Upon excitation, energy transfer from Mn^{2+} to the organic moieties may occur, potentially reducing luminescent efficiency.[39] As shown in the excited state density plots of (But-bz)MnBr$_4$ and (Pent-bz)MnBr$_4$ (Fig. S7d and e‡), the excited electrons and holes are localized

on [MnBr$_4$]$^{2-}$, facilitating highly efficient radiative recombination and near-unity PLQYs. Conversely, in the excited state of (Hex-bz)MnBr$_4$ (Fig. S7f‡), electron transfer from Mn^{2+} to the organic moiety leads to significant non-radiative recombination and inferior PLQY. For comparative analysis, we synthesized (Hex-bz)MnBr$_4$·MeOH crystal containing methanol molecule. The crystal structure of (Hex-bz)MnBr$_4$·MeOH is depicted in Fig. S8.‡ As shown in Table S3,‡ the (Hex-bz)MnBr$_4$ crystal exhibits the lowest radiative decay rate and the highest non-radiative decay rate, likely due to the flexible bridging chain that increases thermal vibrational relaxation and enhances electron transfer. In contrast, the introduction of hydrogen bonding in the (Hex-bz)MnBr$_4$·MeOH crystal suppresses various non-radiative recombination processes, resulting in a higher PLQY. Although the longer alkyl chain in (Hex-bz) MnBr$_4$ allows for lower processing temperature and improved stability of the corresponding melt-quenched glass, it adversely affects the electronic structure, leading to a lower PLQY. Therefore, it is imperative to modify the bisphosphonium cation to achieve a balance between stability, luminescence efficiency, and a lower melting point.

Fluorine is the most electronegative element, and its introduction can significantly alter the electronic configuration. Its presence also influences the atoms to which it is bonded, thereby modulating intermolecular interactions and affecting molecular packing, which impacts melting points.

In this study, we selected three di-fluoro-substituted bromobenzyl compounds: 3,4-difluorobenzyl bromide, 2,3-difluorobenzyl bromide, and 2,6-difluorobenzyl bromide to

prepare BisPP-Br and (BisPP)MnBr$_4$ (Fig. S9‡). Under identical reaction conditions, each di-fluoro-substituted bromobenzyl underwent nucleophilic substitution reactions with 1,6-bis(di-phenylphosphino)hexane, yielding the desired bisphosphonium bromides. Subsequently, the bisphosphonium bromides reacted with MnBr$_2$·4H$_2$O through a solvothermal method to obtain the bisphosphonium metal halides, denoted as (Hex-3,4-2F)MnBr$_4$·MeOH, (Hex-2,3-2F)MnBr$_4$·MeOH, and (Hex-2,6-2F)MnBr$_4$·MeOH. The crystal structures of these three crystals are shown in Fig. 3a and S10a and b,‡ with crystallographic data provided in Table S4.‡ It is noteworthy that the crystal structures of all three crystals are similar, all containing crystalline methanol (Fig. 3b). The experimental XRD pattern of the crystals confirms the accuracy of the structural refinement results (Fig. S11‡). As shown in the DSC curves in Fig. 3c, the melting points of (Hex-3,4-2F)MnBr$_4$·MeOH, (Hex-2,3-2F)MnBr$_4$·MeOH and (Hex-2,6-2F)MnBr$_4$·MeOH crystals are 180, 197, and 208 °C, respectively. In contrast, the unmodified (Hex-bz)MnBr$_4$ exhibits a higher melting point of 225 °C, indicating a decrease in melting points for the fluorinated derivatives. Moreover, the glass transition temperatures of the fluorinated derivatives

remain at around 100 °C, endowing them with excellent glass-forming ability. A comparison of the T_{rg} with other materials is provided in Table S5.‡ To our knowledge, the T_{rg} of (Hex-3,4-2F)MnBr$_4$·MeOH marks the highest value among the reported OIMHs, surpassing even the SiO$_2$ (~0.73). Under the excitation of 360 nm light, all three crystals exhibit similar green light emission, which is also observed in their corresponding melt-quenched glasses (Fig. 3d). The FTIR spectra of the crystals and the glasses indicate that the melt-quenched glasses possess the same organic cations as the crystals. Notably, the peak at 1500 cm^{-1} shifts due to the varying substitution positions of fluorine atoms (see Fig. S12‡). Raman spectra in Fig. S13‡ suggest that the melt-quenched glasses possess the same [MnBr$_4$]$^{2-}$ moieties as the crystals. Additionally, the PLE spectrum of the glass in Fig. S14‡ confirms that Mn ions serve as the luminescent centers. When compared to the original (Hex-bz) MnBr$_4$, the (Hex-3,4-2F)MnBr$_4$·MeOH, (Hex-2,3-2F)MnBr$_4$-·MeOH, and (Hex-2,6-2F)MnBr$_4$·MeOH crystals exhibit enhanced PLQYs of 91.6%, 76.7%, and 85.0%, respectively (Fig. S15‡). Moreover, their melt-quenched glasses also demonstrate an increase of PLQY in comparison with the glass
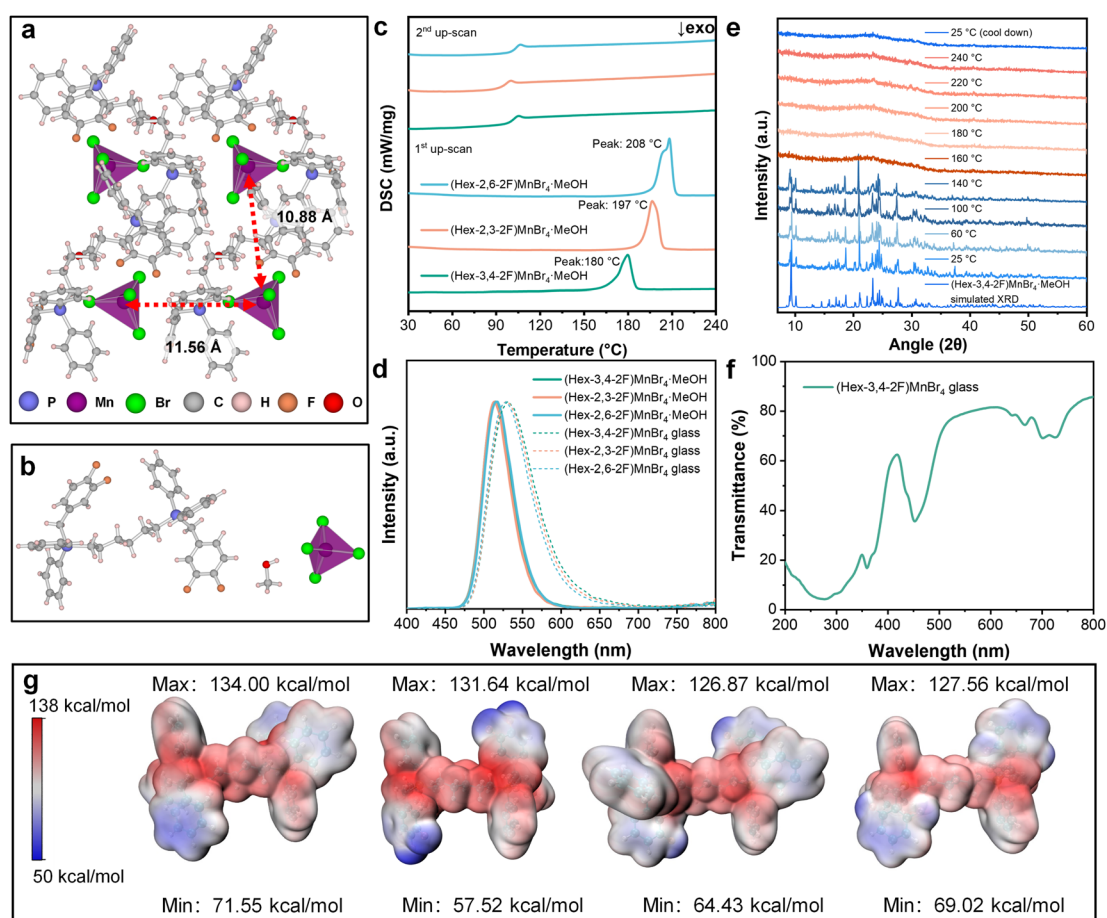

Fig. 3 (a) Crystal structure of (Hex-3,4-2F)MnBr$_4$·MeOH(grey: C, pink: H, blue: P, purple: Mn, green: Br, orange: F, Red: O). (b) The asymmetric unit of (Hex-3,4-2F)MnBr$_4$·MeOH crystal. (c) DSC curves of the crystals, showing the first and second heating processes. (d) The emission spectra of the crystals and glasses under 360 nm excitation. (e) Temperature-dependent XRD patterns of (Hex-3,4-2F)MnBr$_4$·MeOH. (f) UV-Vis transmittance spectrum of (Hex-3,4-2F)MnBr$_4$ glass. (g) Visualization of the electrostatic potential on the molecular surface, with molecules listed sequentially from left to right as Hex-bz, Hex-3,4-2F, Hex-2,3-2F, Hex-2,6-2F.

derived from (Hex-bz)MnBr$_4$ (Table S6‡). The mechanism behind the PLQY improvement will be discussed in the subsequent text.

First, we investigated the influence of the solvent molecule within the crystal. Taking (Hex-3,4-2F)MnBr$_4$·MeOH as an example, we explored the structural changes of the crystal during the melting process. As shown in Fig. 3e, we conducted temperature-dependent X-ray diffraction tests. The results reveal that near the melting point, the crystal undergoes a phase transition from the crystalline state to the amorphous state, corresponding to the solid-to-liquid transformation. Upon cooling to room temperature, the melt is frozen and retains its amorphous nature, giving rise to the formation of amorphous glass. Meanwhile, we conducted the thermogravimetric-infrared (TG-IR) experiment to investigate the melting behavior. During the melting process from 140 to 190 °C, methanol was identified as the decomposing gaseous product(Fig. S16‡). The weight loss (3.02%) observed on the TG curve agrees with the theoretical content (2.87%) of methanol within the crystal (Fig. S17‡). In addition, the solid–liquid transition had been visually confirmed (Fig. S18‡). Consequently, the removal of solvent facilitates the transition from crystal to the amorphous state, which also implies that the resulting glass possesses enhanced stability, as the reversion of glass to the crystalline state requires the involvement of the same solvent.[40] Fig. S19a–c‡ confirm that the OIMH glasses based on fluorine-substituted organic cations do not undergo recrystallization upon heating, demonstrating exceptional thermal stability against recrystallization. The (Hex-bz)MnBr$_4$·MeOH crystal containing methanol molecule was used for comparison. Despite the DSC curve of (Hex-bz)MnBr$_4$·MeOH exhibiting a lower endothermic peak than that of (Hex-3,4-2F)MnBr$_4$ without methanol (Fig. S20‡), temperature-dependent XRD test revealed that during the heating process, (Hex-bz)MnBr$_4$·MeOH first underwent a solvent removal before transforming into the solvent-free (Hex-bz)MnBr$_4$ state (Fig. S21a‡). In contrast, (Hex-bz)MnBr$_4$ without methanol maintains its crystalline state until melting (Fig. S21b‡). Therefore, the presence of methanol within the present OIMH crystal implies that the crystallization of this compound requires the participation of solvent molecules to support the crystal structure. In other words, the recrystallization of (Hex-bz)MnBr$_4$·MeOH and (Hex-3,4-2F)MnBr$_4$·MeOH can be largely suppressed and hence guarantees the higher stability of the corresponding glass. It is worth noting that the prepared (Hex-3,4-2F)MnBr$_4$ glass exhibits bright green emission and high transparency in the visible region (Fig. 3f and S22‡), indicating its potential to work as an excellent scintillator.

The subsequent discussion delves into the impact of fluorine substitution. The introduction of fluorine would significantly influence the distribution of molecular surface electrostatic potential due to its high electronegativity. For systems that are predominantly governed by electrostatic interactions, various physical properties can be analytically interpreted through electrostatic potential.[41] In the case of ionic crystals, the electrostatic potential directly affects the lattice energy, consequently influencing the melting point.[42] As shown in Fig. 3g, a comparison of the surface electrostatic potentials of Hex-bz and di-fluorine-substituted variants (Hex-3,4-2F, Hex-2,3-2F, Hex-2,6-2F) reveals a decrease in the minimum values of surface electrostatic potential following the fluorine substitution. This reduction may weaken the interactions between cations and anions, potentially lowering the material's melting point.[43] Fig. S23‡ illustrates the surface electrostatic potential distribution of organic cations. As the fluorine substitution positions move away from the positive charge center (P core), the minimum surface electrostatic potential decreases. This phenomenon may facilitate the reduction of cation–cation repulsion, thereby decreasing the liquid-phase enthalpy and often leading to a decrease in melting point.[42] To confirm the role of fluorine in lowering the melting point, we synthesized the solvent-free (But-3,4-2F)MnBr$_4$ with a shorter alkyl chain between the two phosphonium cores (see Fig. S24‡). The DSC curve in Fig. S25‡ delivers a melting point of 245 °C, significantly lower than that of the unmodified (But-bz)MnBr$_4$ (281 °C).

The enhanced PLQY in the fluorine-substituted crystals is intricately controlled by the methanol solvent within the crystal and fluorine substitution. Hirshfeld analysis of (Hex-bz)MnBr$_4$·MeOH and (Hex-3,4-2F)MnBr$_4$·MeOH reveals that a strong interaction exists between [MnBr$_4$]$^{2-}$ tetrahedron and methanol (Fig. S26‡). The strong interaction reduces the non-radiative relaxation induced by the thermal vibrations of the [MnBr$_4$]$^{2-}$ tetrahedron, consequently leading to the improvement in PLQY.[44] The peaks in the bottom-left corner of the fingerprint plots suggest similar hydrogen bonding interactions in both crystals. However, the crystals show different degrees of enhancement in PLQY, indicating that the improvement in crystal PLQY is not solely governed by the solvent. The introduction of fluorine alters the surface electrostatic potential of the molecules and affects the dipole moment of the cations. This effect may inhibit Förster resonance energy transfer between organic cations and [MnBr$_4$]$^{2-}$ anion, preventing energy loss and consequently enhancing the PLQY.[39] In the case of the melt-quenched glass, methanol molecules have been removed, indicating that the increased PLQY of fluorine-modified glass is likely attributed to fluorine modification.

(Hex-3,4-2F)MnBr$_4$·MeOH, with the lowest melting point, high glass stability, and outstanding luminescent properties, prompts us to explore its application in X-ray detection and imaging. The key performance parameters of scintillators include light yield (LY), limit of detection (LOD), and imaging resolution. We measured the light yield by comparing the samples with commercial scintillators. LuAG: Ce served as the primary reference scintillator (LY = 25 000 ph MeV^{-1}), while BGO (LY = 8600 ph MeV^{-1}) was used as a secondary reference. The samples and references, having the same size and geometric shape, were placed in quartz dishes, which were then placed inside an integrating sphere and subjected to X-ray irradiation. The emitted photons were fully collected to obtain the absolute light intensity. The obtained light intensity was corrected through X-ray attenuation efficiency, yielding the
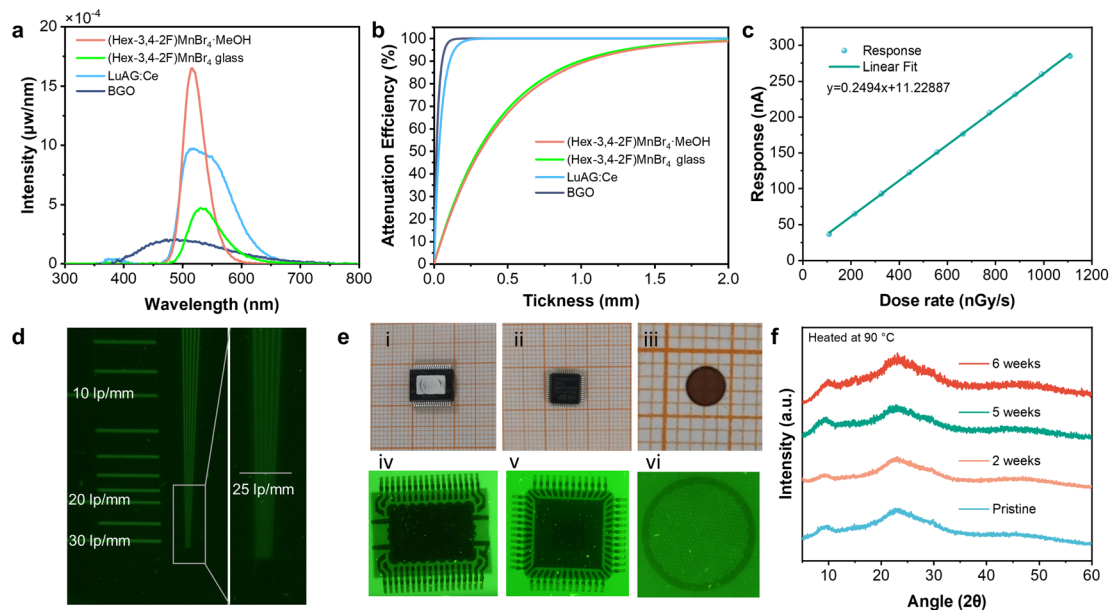
Fig. 4 (a) The emission energy spectra of standard scintillators and (Hex-3,4-2F)MnBr$_4$·MeOH crystal and (Hex-3,4-2F)MnBr$_4$ glass under the excitation of X-ray. (b) Comparison of the attenuation efficiency under 22 keV X-ray irradiation for standard scintillators and (Hex-3,4-2F) MnBr$_4$·MeOH crystal and (Hex-3,4-2F)MnBr$_4$ glass. The attenuation efficiency data were acquired from XCOM database. (c) The linear response of (Hex-3,4-2F)MnBr$_4$ glass to X-ray at different dose rates. (d) An X-ray image of a lead-made line pair card; (e) [i], [ii],[iii] photographs taken under the ambient light; [iv], [v],[vi]photographs taken under X-ray irradiation. (f) The XRD patterns of the (Hex-3,4-2F)MnBr$_4$ glass after continuous heat treatment.

corrected light yields of 20 900 and 9400 ph MeV^{-1} for the (Hex-3,4-2F)MnBr$_4$·MeOH crystal and (Hex-3,4-2F)MnBr$_4$ glass, respectively (Fig. 4a and b), representing 2.43 and 1.09 times that of BGO. Subsequently, we recorded the light output under varying low-dose-rate X-ray irradiation using a photomultiplier tube. As shown in Fig. 4c, the light output of the (Hex-3,4-2F) MnBr$_4$ glass exhibits a good linear response to incident X-rays and delivers a detection limit as low as 64.6 nGy s^{-1}, well below the standard for medical imaging (5500 nGy s^{-1}).

We then conducted a conceptual demonstration of (Hex-3,4-2F)MnBr$_4$ glass for application in X-ray imaging, and a custom X-ray imaging system was built by combining a portable X-ray source, scintillation screen, reflector, and camera. The X-ray image of a line pair card shows a high spatial resolution of 25 line pairs per millimeter (Fig. 4d). This spatial resolution is competitive with various metal halide glasses (Table S7‡). As demonstrated in Fig. 4e, the pins of the chip (the spacing between two pins is 0.5 mm) and the wires connecting the pins can be clearly distinguished. The copper mesh used for transmission electron microscopy (TEM) testing, with a frame width of approximately 20 μm, also exhibits distinguishable structures, highlighting its potential for high-quality X-ray imaging. The thermal stability of glassy scintillators against recrystallization-induced devitrification is important for long-term X-ray imaging applications. It is noteworthy that the (Hex-3,4-2F)MnBr$_4$ glass maintains its transparent and amorphous nature even after being heated at 90 °C for six weeks due to the suppressed recrystallization trend (see Fig. 4f and S27‡), showing exceptional thermal stability and highlighting the potential in high-temperature X-ray imaging.

Conclusions

In conclusion, we have developed a series of Mn-based OIMHs with strong glass-forming ability. By employing bulky bisphosphonium cations as templates, effective segregation of Mn luminescent centers is achieved, leading to a high PLQY of nearly 100%. Due to the rigidity of the bisphosphonium framework, all OIMH amorphous glasses exhibit glass transition temperatures around 100 °C, demonstrating exceptional thermal stability. By extending the alkyl chains between the two phosphorus cores in the cation, we successfully lowered the melting point of the resulting OIMH from 281 °C to 225 °C. Additionally, employing a fluorine-substitution strategy further reduced the melting point to 180 °C while preserving a high T_g, ultimately achieving the highest T_{rg} value of 0.82 among the reported OIMH materials. The glass obtained through melt-quenching (Hex-3,4-2F)MnBr$_4$·MeOH crystal exhibits a high PLQY of 47.6% and an impressive X-ray spatial resolution of up to 25 lp mm^{-1}. The bisphosphonium-based OIMH represents a category of materials with enhanced environmental resilience. The numerous modifiable sites on the bisphosphonium offer ample opportunities for the functionalized design of OIMH glasses, such as designing bisphosphoniums with thermally activated delayed fluorescence characteristics. In summary, this halide-substituted bisphosphonium cation strategy for constructing OIMH glass with low melting temperature, high PLQY, and transparent appearance can be extended to other families of OIMH materials, paving the way for various applications such as light emitting diode (LED), X-ray detection and imaging, optical communication and sensors.

Data availability

The data supporting the findings of this paper are available from the corresponding author upon reasonable request.

Author contributions

D.-B. K. and J.-B. L. conceived and designed the experiments. J.-B. L. performed material synthesis, measurements, and data analysis. J.-H. W., Z.-L. H., J.-H. C., Q.-P. P., and Z.-Z. Z. assisted with scintillation properties measurements and data analysis. J.-H. C. aided in thermodynamics measurements and data analysis. All authors contributed to the discussion of data and the writing of the manuscript.

Conflicts of interest

There are no conflicts to declare.

Acknowledgements

References

1 L. Yi, B. Hou, H. Zhao and X. Liu, *Nature*, 2023, **618**, 281–286.

2 X. He, Y. Deng, D. Ouyang, N. Zhang, J. Wang, A. A. Murthy, I. Spanopoulos, S. M. Islam, Q. Tu, G. Xing, Y. Li, V. P. David and T. Zhai, *Chem. Rev.*, 2023, **123**, 1207–1261.

3 F. Zhou, Z. Li, W. Lan, Q. Wang, L. Ding and Z. Jin, *Small Methods*, 2020, **4**, 2000506.

4 H. Wu, Y. Ge, G. Niu and J. Tang, *Matter*, 2021, **4**, 144–163.

5 J.-H. Wei, J.-F. Liao, X.-D. Wang, L. Zhou, Y. Jiang and D.-B. Kuang, *Matter*, 2020, **3**, 892–903.

6 G. Kakavelakis, M. Gedda, A. Panagiotopoulos, E. Kymakis, T. D. Anthopoulos and K. Petridis, *Adv. Sci.*, 2020, **7**, 2002098.

7 Y. Zhou, J. Chen, O. M. Bakr and O. F. Mohammed, *ACS Energy Lett.*, 2021, **6**, 739–768.

8 H. Tsai, S. Shrestha, R. A. Vilá, W. Huang, C. Liu, C.-H. Hou, H.-H. Huang, X. Wen, M. Li, G. Wiederrecht, Y. Cui, M. Cotlet, X. Zhang, X. Ma and W. Nie, *Nat. Photonics*, 2021, **15**, 843–849.

9 Y. He, M. Petryk, Z. Liu, D. G. Chica, I. Hadar, C. Leak, W. Ke, I. Spanopoulos, W. Lin, D. Y. Chung, B. W. Wessels, Z. He and M. G. Kanatzidis, *Nat. Photonics*, 2021, **15**, 36–42.

10 M. L. Zaffalon, F. Cova, M. Liu, A. Cemmi, I. Di Sarcina, F. Rossi, F. Carulli, A. Erroi, C. Rodà, J. Perego, A. Comotti, M. Fasoli, F. Meinardi, L. Li, A. Vedda and S. Brovelli, *Nat. Photonics*, 2022, **16**, 860–868.

11 Y. Wang, M. Li, Z. Chai, Y. Wang and S. Wang, *Angew. Chem., Int. Ed.*, 2023, **62**, e202304638.

12 C. Zhou, L. J. Xu, S. Lee, H. Lin and B. Ma, *Adv. Opt. Mater.*, 2020, **9**, 2001766.

13 G. Zhou, B. Su, J. Huang, Q. Zhang and Z. Xia, *Mater. Sci. Eng., R*, 2020, **141**, 100548.

14 C. Dong, X. Song, B. E. Hasanov, Y. Yuan, L. Gutiérrez-Arzaluz, P. Yuan, S. Nematulloev, M. Bayindir, O. F. Mohammed and O. M. Bakr, *J. Am. Chem. Soc.*, 2024, **146**, 7373–7385.

15 J.-H. Wei, J.-F. Liao, L. Zhou, J.-B. Luo, X.-D. Wang and D.-B. Kuang, *Sci. Adv.*, 2021, **7**, eabg3989.

16 D.-Y. Li, H.-Y. Kang, Y.-H. Liu, J. Zhang, C.-Y. Yue, D. Yan and X.-W. Lei, *Chem. Sci.*, 2024, **15**, 953–963.

17 Y. Qin, P. She, X. Huang, W. Huang and Q. Zhao, *Coord. Chem. Rev.*, 2020, **416**, 213331.

18 Z. Z. Zhang, J. H. Wei, J. B. Luo, X. D. Wang, Z. L. He and D. B. Kuang, *ACS Appl. Mater. Interfaces*, 2022, **14**, 47913–47921.

19 Z. L. He, J. H. Wei, Z. Z. Zhang, J. B. Luo and D. B. Kuang, *Adv. Opt. Mater.*, 2023, **11**, 2300449.

20 W. Zhang, P. Sui, W. Zheng, L. Li, S. Wang, P. Huang, W. Zhang, Q. Zhang, Y. Yu and X. Chen, *Angew. Chem., Int. Ed.*, 2023, **62**, e202309230.

21 C. Ye, L. N. McHugh, C. Chen, S. E. Dutton and T. D. Bennett, *Angew. Chem., Int. Ed.*, 2023, **62**, e202302406.

22 B. K. Shaw, A. R. Hughes, M. Ducamp, S. Moss, A. Debnath, A. F. Sapnik, M. F. Thorne, L. N. McHugh, A. Pugliese, D. S. Keeble, P. Chater, J. M. Bermudez-Garcia, X. Moya, S. K. Saha, D. A. Keen, F. X. Coudert, F. Blanc and T. D. Bennett, *Nat. Chem.*, 2021, **13**, 778–785.

23 J. B. Luo, J. H. Wei, Z. Z. Zhang, Z. L. He and D. B. Kuang, *Angew. Chem., Int. Ed.*, 2023, **62**, e202216504.

24 Z. Z. Zhang, Z. L. He, J. B. Luo, J. H. Wei, X. X. Guo, J. H. Chen and D. B. Kuang, *Adv. Opt. Mater.*, 2024, **12**, 2302434.

25 Z. L. He, J. H. Wei, J. B. Luo, Z. Z. Zhang, J. H. Chen, X. X. Guo and D. B. Kuang, *Laser Photonics Rev.*, 2024, **18**, 2301249.

26 R. Zhang, H. Xie, W. Liu, K. Zhan, H. Liu, Z. Tang and C. Yang, *ACS Appl. Mater. Interfaces*, 2023, **15**, 47238–47249.

27 Y. Xu, Z. Li, G. Peng, F. Qiu, Z. Li, Y. Lei, Y. Deng, H. Wang, Z. Liu and Z. Jin, *Adv. Opt. Mater.*, 2023, **11**, 2300216.

28 V. Morad, I. Cherniukh, L. Pottschacher, Y. Shynkarenko, S. Yakunin and M. V. Kovalenko, *Chem. Mater.*, 2019, **31**, 10161–10169.

29 B. Li, J. Jin, M. Yin, K. Han, Y. Zhang, X. Zhang, A. Zhang, Z. Xia and Y. Xu, *Chem. Sci.*, 2023, **14**, 12238–12245.

30 A. Inoue, *Acta Mater.*, 2000, **48**, 279–306.

31 D. Turnbull, *J. Chem. Phys.*, 1952, **20**, 411–424.

32 D. Turnbull, *Metall. Trans. B*, 1981, **12**, 217–230.

33 D. Turnbull, *Contemp. Phys.*, 1969, **10**, 473–488.

34 G. J. Fan, H. Choo and P. K. Liaw, *J. Non-Cryst. Solids*, 2007, **353**, 102–107.

35 A. Singh and D. B. Mitzi, *ACS Mater. Lett.*, 2022, **4**, 1840–1847.

36 L. J. Xu, X. Lin, Q. He, M. Worku and B. Ma, *Nat. Commun.*, 2020, **11**, 4329.

37 A. Singh, M. K. Jana and D. B. Mitzi, *Adv. Mater.*, 2021, **33**, e2005868.

38 J. Lin, M. Zhang, N. Sun, S. He, X. Zhang, Z. Guo, J. Zhao, Q. Liu and W. Yuan, *J. Mater. Chem. C*, 2022, **10**, 16773–16780.

39 S. Zhang, Y. Zhao, Y. Zhou, M. Li, W. Wang, H. Ming, X. Jing and S. Ye, *J. Phys. Chem. Lett.*, 2021, **12**, 8692–8698.

40 Y.-S. Wei, Z. Fan, C. Luo and S. Horike, *Nat. Synth.*, 2023, **3**, 214–223.

41 X. Liu, K. E. O'Harra, J. E. Bara and C. H. Turner, *J. Phys. Chem. B*, 2021, **125**, 3653–3664.

42 B. D. Rabideau, M. Soltani, R. A. Parker, B. Siu, E. A. Salter, A. Wierzbicki, K. N. West and J. H. Davis, *Phys. Chem. Chem. Phys.*, 2020, **22**, 12301–12311.

43 N. Mohan and C. H. Suresh, *J. Phys. Chem. A*, 2014, **118**, 1697–1705.

44 L.-K. Gong, Q.-Q. Hu, F.-Q. Huang, Z.-Z. Zhang, N.-N. Shen, B. Hu, Y. Song, Z.-P. Wang, K.-Z. Du and X.-Y. Huang, *Chem. Commun.*, 2019, **55**, 7303–7306.